

Chapter 1

Introduction

1.1 Towards the characterization of exoplanets

The field of exoplanetary science is rapidly accelerating with large scientific and instrumental investments undertaken, with the ultimate goal of detecting and characterizing an Earth-like planet, with the potential for life (as we know it). Since the very first exoplanet detection¹ (Mayor et al., 1995) the number of confirmed² exoplanets has grown to over 3790 with almost another 3000 candidates awaiting confirmation³. However, simply detecting the presence of exoplanets is not nearly enough to satisfy our quest for knowledge. There is an exorbitant amount to be gained through the full characterization of these known exoplanets: density, composition, internal structure, atmosphere properties, and surface temperature.

When an Earth-twin planet is suspected (there have been several false claims already (e.g. Mullally et al., 2018) **more other earth like planets shown to not be earth like or redacted papers**) a full characterization is required to confirm its habitability ([ref](#)). For instance, knowing only the mass and radius can provide an average density but not the composition or the internal structure [ref](#) [cite a paper about composition degeneracy](#). The presence of an exoplanet's atmosphere will also influence the average density but can provide detectable clues on the planet's composition. Several techniques being explored to detect and characterize exoplanet atmospheres (e.g. Snellen et al., 2010; Martins et al., 2016; Piskorz et al., 2016) [a transmission spectroscopy paper](#) with several recent advancements.

In this chapter the common exoplanet and atmospheric detection methods will be introduced, followed by some exoplanet property distributions and the motivation for the work performed in this thesis.

other dead earth-like planets

1.2 Exoplanet detection methods

There are several detection methods used to build up the picture of the current understanding of exoplanet candidates. The methods are often complementary in that they are sensitive to different parameter spaces and are able to contribute different exoplanet properties. The simplest example is that planetary

¹ around a Sun-like star

² Validated by more than one detection method

³ exoplanets.nasa.gov as of October 2018

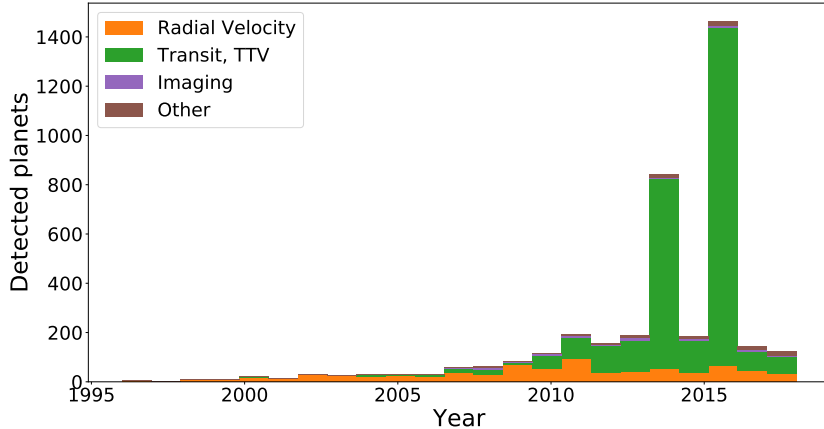


Figure 1.1: Number of exoplanet detections per year separated by method (data from exoplanet.eu October 2018).

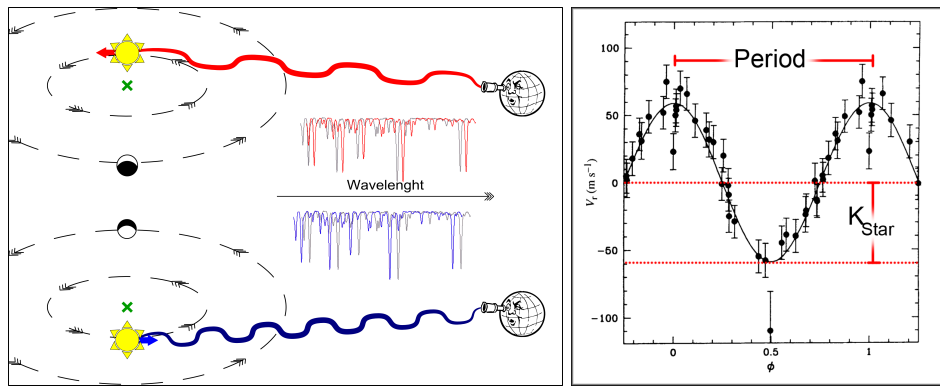


Figure 1.2: Left: Diagram of RV method. Right: RV variation for the detection of 51 Pegasi. Credit: Mayor et al. (1995)

mass and radius are obtained from the radial velocity and transit methods separately. The exoplanet detection rates for different methods since 1995 are shown in Figure 1.1. The detection rates among different methods are not uniform, with the transit method having the majority of detections due to the Kepler space telescope (Borucki et al., 2008). The radial velocity method has a fairly consistent detection rate while direct imaging and other methods have only made a small contribution to the total detection so far.

Details about the various main detection methods are provided in the following sections.

1.2.1 Radial Velocimetry

This technique measures the radial velocity⁴ (RV) of the star by analysing the relative Doppler shift of its spectral lines due to the gravitational interaction with a companion. As the star and companion orbit around their common centre of mass (barycentre) the spectrum of the star periodically oscillates due to the change in relative motion to the observer as depicted in Figure 1.2 (left).

⁴ Velocity projected along line of sight.

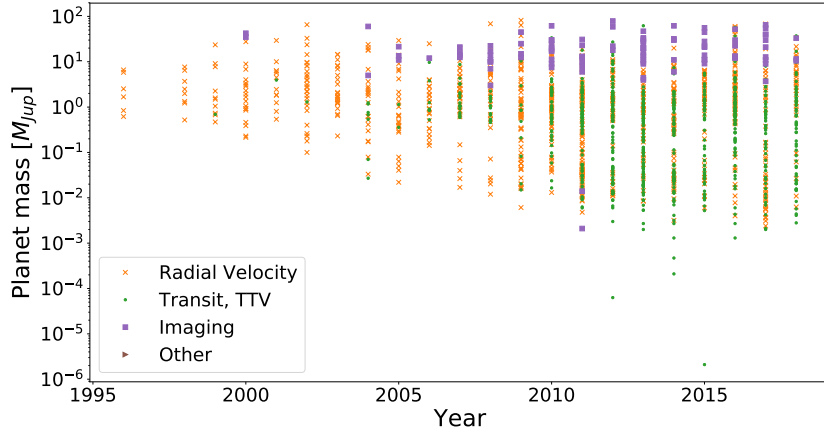


Figure 1.3: Exoplanet discovery year versus exoplanet mass showing a trend towards detecting lower mass planets. Exoplanets without a measured mass are not shown. The colours indicate the initial detection method.

The radial velocity variation, directed along the line of sight, is given by:

$$RV = \gamma + K[\cos(\nu(t, P, T_0, e) + \omega) + e \cos(\omega)] \quad (1.1)$$

where γ is constant barycentre velocity of the system relative to the Sun⁵, K is the velocity semi-amplitude, e the eccentricity, and ω is the argument of periastron. The true anomaly ν , is a function of time t , orbital period P , and the time of periastron passage T_0 , and eccentricity.

The velocity amplitude K of a star of mass M_\star due to a companion with mass M_p with orbital period P , eccentricity e , and inclination⁶ i is (e.g. Cumming et al., 1999):

$$K = \left(\frac{2\pi G}{P} \right)^{1/3} \frac{M_p \sin i}{(M_p + M_\star)^{2/3}} \frac{1}{\sqrt{1 - e^2}}, \quad (1.2)$$

where G is the gravitational constant.

The key exoplanet property determined by the amplitude RV technique is the companion mass, relative to the orbital inclination $M_p \sin i$. As the companion mass is in the numerator of Equation 1.2 the RV technique is more sensitive to larger mass planets. Also since $K \propto P^{-1/3}$ the amplitude is greater for short period close in orbits⁷.

The RV method kick-starting the exoplanet discipline by detecting the first exoplanet around a solar-type star 51 Pegasi (Mayor et al., 1995). The RV curve for 51 Pegasi is shown on the right side of 1.2. The first discoveries were surprising as Jupiter mass planets in short period orbits⁸ were unlike anything in our Solar System. Several exoplanet discoveries followed in quick successions (e.g. Butler et al., 1996; Marcy et al., 1996) with many confirming the existence of the type of planets now referred to as “hot-Jupiters” (Butler et al., 1997; Charbonneau et al., 2000).

The radial velocity amplitudes of the first exoplanets detected were around 60 m s^{-1} while the radial velocity signal of the Earth in a 1 year orbit around a solar-type star however is 8.9 cm s^{-1} (Figueira

⁵ Earth’s barycentre motion is well known and removed.

⁶ Relative to a plane that is tangential to the celestial sphere, $i = 90$ is edge on.

⁷ From Kepler’s Law $P^2 \propto a^3$

⁸ $M_p \sin i = 0.47 \text{ M}_{\text{Jup}}$ orbiting at 0.05 au for 51 Pegasi

et al., 2010). Specially constructed spectrographs, such as HARPS (Mayor et al., 2003) along with improved reduction techniques (Lovis et al., 2007) pushed this mass detection limit down to the m s^{-1} level. ESPRESSO (Pepe et al., 2014; Mégevand et al., 2014) is the next generation high precision optical spectrograph aiming to push the detection limits to 10 cm s^{-1} , to detect an Earth twin. The gradual decrease in measured mass of exoplanets over time is shown in Figure 1.3. The different symbols indicate the detection method, not necessarily the method used to measure the exoplanet mass.

Most RV detection has been performed using optical spectrographs. However, as the amplitude of RV signal is inversely proportional to the mass of the star ($\text{RV} \propto M_{\star}^{-2/3}$), there are dedicated surveys focusing on smaller mass M-dwarf stars (e.g. Reiners et al., 2018). M-dwarfs are inherently cooler and thus emit a majority of their stellar output in the near-infrared; new dedicated high-resolution nIR spectrographs have and are being designed and implemented to meet this demand e.g., CARMENES, NIRPS, SPIRou, CRIRES+.

[cite an M-dwarf paper?](#)

1.2.2 Transit methods

The transit method detects the presence of an exoplanet by observing the periodic dimming of the star due to the passage of the exoplanet between the star and observer, partially blocking the star. Geometry requires the orbit of the exoplanet to be aligned edge-on to the line of sight (low inclinations) for a transit to occur. The geometric probability, P , that a exoplanet transits is estimated by

$$P \approx \frac{R_{\star}}{a(1 - e^2)}, \quad (1.3)$$

where e is the eccentricity of the orbit, R_{\star} is the star radii and a is the semi-major axis of the orbit (star-planet distance) (J. W. Barnes, 2007). The probability of transit increases with the size of the star but decreases with distance to the star.

The drop in stellar brightness during the transit allows the measurement of the planet/star radius ratio:

$$\frac{\Delta L}{L} \sim \left(\frac{R_p}{R_{\star}} \right)^2 \quad (1.4)$$

where L is the luminosity of the star, ΔL is the maximum luminosity variation (transit depth), and R_{\star} and R_p are the radius of the star and planet respectively.

The transit method complements RV measurements as the inclination, i , of the orbit can be determined from the transit. This removes the $\sin i$ ambiguity found in the $M_p \sin i$ of RV detections so the true mass, M_p , of the exoplanet can be revealed. The true mass along with the planet's radius provides a value for the exoplanets average density⁹, hinting at the possible composition.

There are several other astrophysical phenomena which can mimic transiting exoplanet signals, created by configurations of two or more stars which may not involve an exoplanet. For example a transiting low-mass or white-dwarf star, grazing binary stars, or a transit in a multi-star system (see e.g. Cameron, 2012; Santerne et al., 2013). Follow-up RV observations (e.g. Santerne et al., 2011) are usually required to confirm the planets existence. Statistical validation techniques are also possible, such as the PASTIS software (Díaz et al., 2014), when follow-up can not be performed. With RV follow-up, Santerne et al.

⁹ $\rho \equiv \frac{\text{Mass}}{\text{Volume}} = \frac{3}{4\pi} \frac{M_p}{R_p^3}$

(2012) found a false positive rate as high as 35% for short period giant planets, while Santerne et al. (2016b) found a 54.6% false positive rate of 129 giant planet¹ with periods less than 400 days. These sub-sample false positive rates are however higher than the global false positive rate of 9.4% (Fressin et al., 2013)/11.3% (Santerne et al., 2013) found for Kepler. Some of the currently known exoplanet systems with the smallest radii and lightest mass have been detected through transit and later confirmed with high-precision RV follow-up (e.g. Queloz et al., 2009; Pepe et al., 2013; López-Morales et al., 2016; Ment et al., 2018).

The identification of unresolved multiple stars, such as a binary or a² unrelated background star, can be achieved through high-resolution spectroscopy in which the spectral lines of individual stars can be separated (Kolbl et al., 2015). This is important to measure the correct radius³ of exoplanets as the extra light contribution from an unresolved secondary star will reduce the transit depth, mimicking a smaller transiting planet.

The transit of a single planet can not directly determine the planetary mass. However, in multiple planet systems, the masses and sometimes the presence of other planets in the system can be determined from perturbations in the transit time and duration (e.g. Holman et al., 2005; Holman et al., 2010). A large number of systems have been detected that show transit timing variations (TTV) and transit duration variations (TDV) (e.g. Holczer et al., 2016) due to the gravitational interaction between planets. The statistical validity of multi-transiting planets is also higher than single planets as the probability of multiple false positives is lower than having multiple planets in the system (Lissauer et al., 2012), making them easier to validate.

The presence of star spots on the surface of a star can be observed during transit. A star spot is a dark region on the stellar surface due to magnetic fields, which decreases the luminosity slightly. Examples of spots can be seen in the middle of the Sun from an image of the 2012 transit of Venus in Figure 1.4 (left). It shows several dark sunspots alongside Venus, although Venus did not cross them. Unlike for other stars, sunspots are spatially resolved. If an exoplanet passes in front of a spot, the luminosity decrease from the spot is temporarily hidden and a small bump occurs in the transit shape. The presence of spots in successive transits (see Figure 1.4 (right)) can indicate the alignment of the stellar rotation to the planet orbital plane (Sanchis-Ojeda et al., 2013). In this simulation an orbit aligned with the stellar rotation and the transit crosses the spot in four successive orbits. In a misaligned case a spot would only be observed in one transit.

The vast majority of transit detections have come from Kepler (Borucki et al., 2011), which focused on a small patch of sky (0.25%) for four years continuously. However, CoRoT (Barge et al., 2008) and ground-based surveys, such as WASP (Pollacco et al., 2006), OGLE (Udalski et al., 2002), TreS (Alonso et al., 2004) have also had successful transit detections.

Following in Kepler’s footsteps the next generation transit hunter TESS (Ricker et al., 2015) has already announced discoveries of new transiting planets only months after launch (Vanderspek et al., 2018; Gandolfi et al., 2018; Huang et al., 2018a). It will eventually cover more than 90% of the sky with an impressive planetary yield expected of \sim 10 000 exoplanets, with around 3500 the size of Neptune or smaller (Barclay et al., 2018; Huang et al., 2018b). However, the observation coverage is not uniform, with the majority of the ecliptic plane receiving only one month of observations, limiting the detection sensitivity to short period transiting planets. The ecliptic poles will receive almost one year continuous observation.

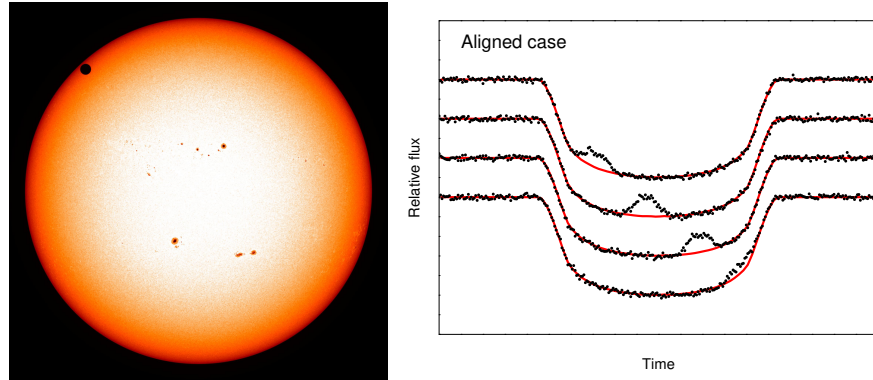


Figure 1.4: Left: Image from the 2012 transit of Venus obtained from the Solar Dynamics Observatory satellite. Venus is the dark circle in the top left of the Sun. Limb darkening is observed as the change in colour/brightness from white to red near the edge. Several sunspots are also observed on the surface of the Sun. Credit: NASA/SDO, HMIR. Right: Simulation of 4 successive transits crossing a star spot with the orbit aligned with the stellar rotation. The stellar rotation is 1/10 the orbital period. Adapted from Sanchis-Ojeda et al. (2013, Figure 1).

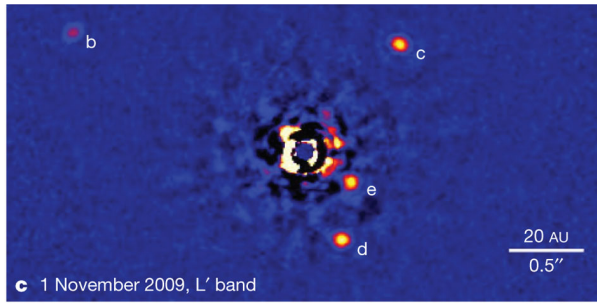


Figure 1.5: Direct detection of four exoplanets around HR 8799 (Marois et al., 2010).

1.2.3 Direct Imaging

The direct imaging technique involves directly imaging an exoplanet in orbit around a star. The first planets directly imaged were 2MASSWJ 1207334–393254 b using adaptive optics with NACO on the VLT (Chauvin et al., 2004), three planets around HR 8799 using angular differential imaging on the Keck and Gemini telescopes (Marois et al., 2008), and Fomalhaut b using chronography on the HST (Kalas et al., 2008). As an example the direct image of HR 8799 is shown in Figure 1.5, where a fourth planet was revealed (Marois et al., 2010).

Direct imaging requires resolving the angular separation between the star and planet and is best suited to detect giant planets in wide orbits (>10 au) around nearby stars. This is shown by the clustering of direct image detections shown in Figure 1.3. Extremely young giants observed in the infrared are favoured as they have higher thermal emission (while they are still cooling) and larger surface area resulting in a higher contrast ratio to the host.

High-contrast adaptive optics instruments, such as SPHERE@VLT (Beuzit et al., 2008) and GPI (Macintosh et al., 2008), are being used with several different techniques to observe targets closer to the star and with smaller contrasts, usually involving blocking or cancelling out the light from the star while keeping the planet (e.g. Marois et al., 2005; Mawet et al., 2005; Schmid et al., 2005; Sirbu et al.,

2017b; Sirbu et al., 2017a; Wang et al., 2017). Ground based direct imaging requires adaptive optics to reduce the turbulence induced by the atmosphere, increasing the angular resolution down to the telescope diffraction limit.

The direct imaging technique is also used to observe circumstellar and protoplanetary disks, and has even captured images of planets during formation (e.g. Sallum et al., 2015). Combining direct images from different photometric bands can allow for the creation of low-resolution exoplanet spectra (e.g. Kuzuhara et al., 2013; Zurlo et al., 2015).

1.2.4 Astrometry

Astrometry measures the precise position of the stars on the plane of the sky. The motion of a star with an exoplanet about its centre of mass can be observed in the periodic oscillating of position from its proper motion in the sky.

For a circular orbit the angle of the semi-major axis of the apparent orbital ellipse, the amplitude of the astrometric signature (θ), is given by

$$\theta = \frac{M_p}{M_{star} + M_p} \frac{a}{d} \quad (1.5)$$

where, M_p and M_\star are the planet and stellar mass, a is the semi-major axis (in au) and d is the distance from the observer to the system (in parsec) (M. Perryman, 2011).

This shows that the astrometric signal is proportional to the companion/star mass ratio and to the orbital radius, a . The amplitude also decreases inversely with distance, as the angles become smaller. This is unlike the RV and transit methods for which the amplitude is not affected by distance. Astrometry is complementary to the RV method as it measures the orbital motion perpendicularly to the line of sight, allowing the three-dimensional orbit to be determined.

A modelled astrometric signal is shown in Figure 1.6, for a star at a distance of 50 pc, with a proper motion of 50 mas yr⁻¹, and orbited by a planet of $M_p = 15 M_{Jup}$, $e = 0.2$, and $a = 0.6$ au (M. A. C. Perryman, 2000). The straight dashed line shows the path of the system's barycentric motion viewed from the Solar System barycentre. The dotted line shows the effect of parallax (the Earth's orbital motion around the Sun, with a period of 1 year). The solid line shows the apparent motion of the star as a result of the planet, the additional perturbation being magnified by $\times 30$ for visibility.

Although astrometry has detected many binary stars (e.g. Gontcharov et al., 2000) and found several brown-dwarf companions (e.g. Sahlmann et al., 2011), the exoplanet discovery's are few. A $1.5 M_{Jup}$ mass planet in a roughly 1000 day orbit around HD 176051 was reported by Mutterspaugh et al. (2010), and recently the astrometric perturbation of a known planet, Beta Pictoris b, was performed utilizing measurements from GAIA (Collaboration et al., 2016) and HIPPARCOS (ESA, 1997) to determine a mass of $11 M_{Jup}$ (Snellen et al., 2018).

The predicted astrometric variations for an exoplanet are at the level of sub-milliarcseconds and therefore are not achievable from the ground due to atmospheric turbulence. The most precise astrometric measurements come from spacecraft. These are currently being performed with GAIA with the recent release of astrometric parameters for 1332 million sources (Collaboration et al., 2018) and reaching a precision of 0.04 mas for the brightest stars (<14 magnitude). Simulations predict that more than 21 000 large mass planets ($1-15 M_{Jup}$) in long-period orbits should be discovered during the 5 year nominal GAIA mission (M. Perryman et al., 2014).

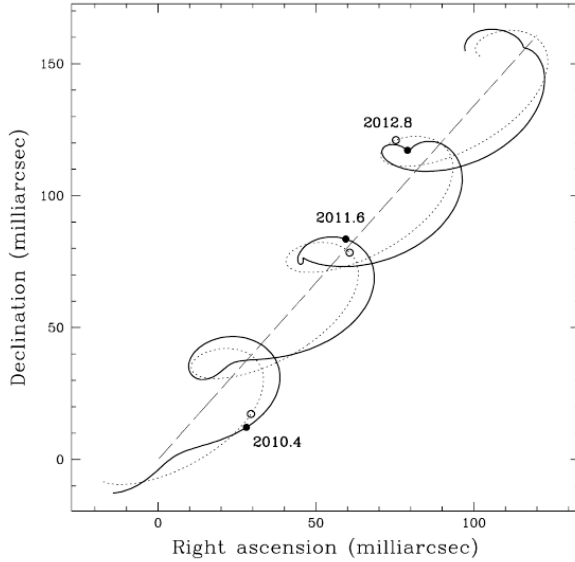


Figure 1.6: The modelled path on the sky from M. A. C. Perryman (2000). Showing a star at a distance of 50 pc, with a proper motion of 50 mas yr^{-1} , and orbited by a planet of $M_p = 15 M_{\text{Jup}}$, $e = 0.2$, and $a = 0.6 \text{ au}$. The straight dashed line shows the path of the system's barycentric motion viewed from the Solar System barycentre. The dotted line shows the effect of parallax (the Earth's orbital motion around the Sun, with a period of 1 year). The solid line shows the apparent motion of the star as a result of the planet, the additional perturbation being magnified by $\times 30$ for visibility.

1.2.5 Microlensing

Microlensing is an astronomical effect predicted by Einstein's General Theory of Relativity. The mass of an object bends space-time which causes light to be visibly deflected around large mass objects. As a star passes between Earth and a distant star it acts like a lens, bending and magnifying the light from the background star. The gravitation of a planet orbiting the lens star (if it exists) creates a distortion in the lens, leading to small caustics, deviations in the microlensing light curve for a single lens event (star without a planet).

An example is shown in Figure 1.7 where a lensing magnification of up to $\times 3$ is observed for OGLE2005-BLG-390 (Beaulieu et al., 2006). On the falling edge of the lensing event (and inset top right) there is a bump due to the presence of a $5.5 M_{\text{Jup}}$ companion.

The difficulties of microlensing is that they require the chance alignment between Earth, a nearby lens star, and a distance source star, which is unrepeatable. Some caustics are often difficult to fit and yield degenerate results, making characterization of the planet difficult. Follow-up measurements of a handful of microlensing events have been performed (e.g. Kubas et al., 2012; Batista et al., 2015; Santerne et al., 2016a) to break degeneracies. However, follow-up can be difficult as microlensing is sensitive to distant host stars, which are outside the ability of current spectrographs. It is also sensitive to planets with a wider orbital separation compared to transits and RV. Currently there are 82 planets in 79 systems detected by microlensing, as listed in the exoplanet.eu database.

Microlensing events are detected and monitored using dedicated global telescope networks such as OGLE, MOA, microFUN and PLANET. They focus their viewing towards the galactic bulge where there are more stars and a higher chance for microlensing events to occur.

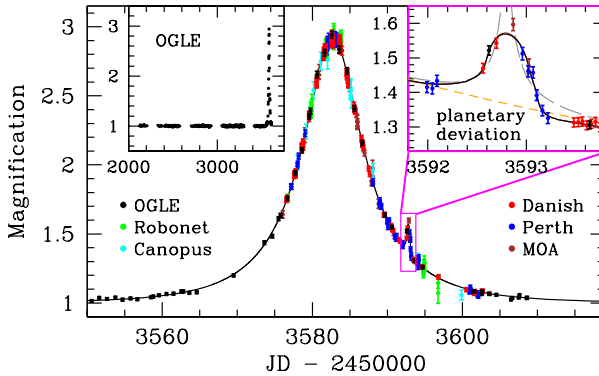


Figure 1.7: Microlensing magnification of OGLE2005-BLG-390 from (Beaulieu et al., 2006). The presence of the $5.5 M_{\text{Jup}}$ planet causes the small bump shown in the upper right inset plot.

The precise stellar proper motions from the GAIA mission are being used to predict possible future alignments that could produce microlensing events (Klüter et al., 2018)

1.2.6 Pulsar timing

Pulsars are rapidly rotating neutron stars or white dwarfs formed after the death of a giant star, that radiate an intense electromagnetic beam. The timing variations of the millisecond pulsar¹⁰ PSR1257+12 led to the first extrasolar planet detection (Wolszczan et al., 1992). There are two models of planet formation around pulsars: either they formed before the supernova explosion and survived, or they formed after, from the remnants of the supernova (Starovoit et al., 2017). There is still a rarity of less than 10 pulsars with known orbiting planets.

1.3 Detecting atmospheres

To help characterize an exoplanet, a detection of its atmosphere can provide useful information. After the detection of exoplanets and the measurement of their bulk properties, detecting their atmospheres is the next step. The detection of planetary atmosphere is difficult due to the low planet-to-star flux ratio. This requires high precision instrumentation to detect. For example the planet-to-star flux ratio in the optical is $\approx 10^{-4}$ for a hot Jupiter with a 3 day orbit, in which the main component is reflected star light. In the infrared the thermal emission of the planet dominates and the flux ratio rises to $\approx 10^{-3}$. These flux ratios require observations with signal-to-noise ratios of 10^4 and 10^3 in the optical and infrared respectively to achieve a planetary signal at the same level as the noise level. Only just at the capabilities of the current generation of technology, and with very long observation cost.

Several photometric and high-resolution spectroscopic techniques are showing promising results; detailed in the following sections.

1.3.1 Occultation and phase variations

Secondary transit and phase variations are an extension of the transit method, requiring higher precision to detect the reflection and thermal emission of the exoplanet. The observed light curve is analysed

¹⁰ Rotating at 9 650 revolutions per minute

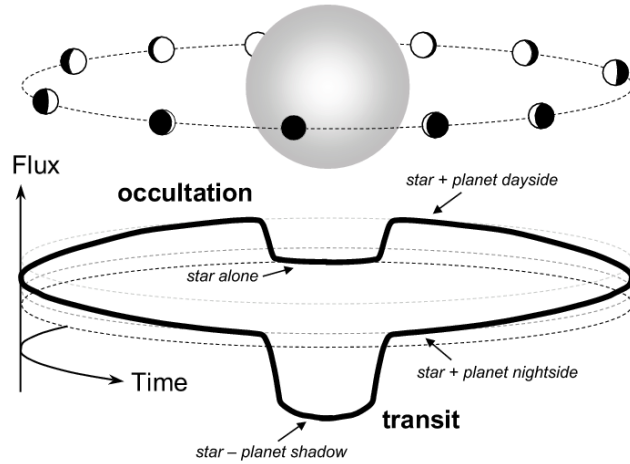


Figure 1.8: Illustration of the flux contribution from a star and planet in a transiting exoplanet system throughout its orbit. Credit Winn (2010).

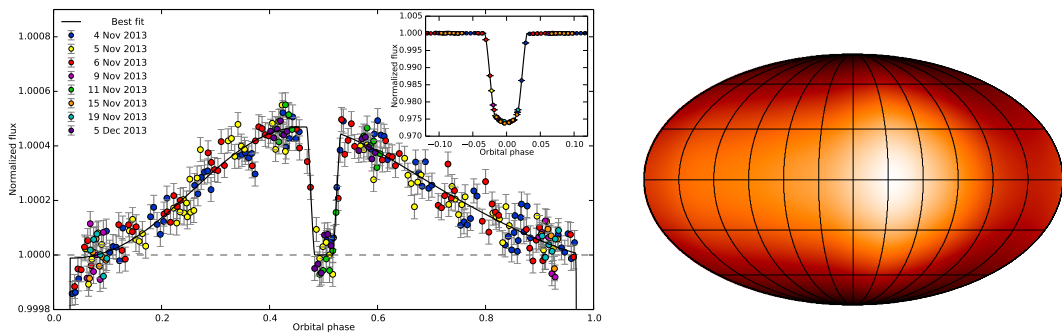


Figure 1.9: Left: Band integrated phase variation of WASP-43b from the HST (Stevenson et al., 2014). The primary transit is inset top right. The peak of brightness occurs before the secondary transit. Right: Global temperature map of the hot Jupiter HD 189733b obtained with Spitzer Space Telescope (Knutson et al., 2007a). The hottest point is offset from the sub-stellar point with the day side and night side temperatures around 930 K and 650 K respectively.

considering it has two components, not only light from the star but also light from the planet, albeit at a much lower flux level. To help visualize and discuss the components of exoplanet atmospheres Figure 1.8 is provided showing a transiting planet in orbit around a star, in which the planet also passes behind the star causing an occultation. The planet is shown at several positions of the orbit indicating the proportion of day side and night side observed. Below the star and planet is a diagram showing the changing flux variation (solid black line) over time, following the orbit. If the orbital alignment is such that the planet will pass behind the star it will cause an occultation of the planet. At this point the only light received is from the star alone, creating a baseline stellar measurement. While during the primary transit there is also a small thermal emission contribution from the night side of the planet, as well as it partially blocking the star.

Throughout the orbit of the planet there is a variation in the planetary flux due to the alternating day/night side of the planet observed. There are multiple components of the planetary flux, reflection and emission, that can be analysed with multi-band phase curves (e.g. Knutson, 2009; Esteves et al., 2013). Optical phase curves will mostly show the reflected light from the day side of the planet, allowing modelling the atmospheric albedo (fraction of light reflected by the atmosphere), and can provide details on the atmospheric scattering (Madhusudhan et al., 2012) and aerosol composition (Oreshenko et al., 2016) through the optical phase function (day/night fraction). Thermal emission of the planet will provide stronger modulation of infrared phase curves and can provide insights into the atmospheres thermal structure and heat circulation (Goodman, 2009; Koll et al., 2016).

An example of phase variations in the infrared spectra of WASP-43b obtained with the Hubble Space telescope is given in Figure 1.9 (left). The large amplitude of phase variation between the day and night side indicates that the night side is much cooler and there is an inefficient heat circularity from the day to night side. A planet with an efficient day/night heat distribution mechanism would quickly equalize and have smaller phase variation. One key observable from Figure 1.9 is that the peak of the phase variation is offset from the location of the secondary transit. The hottest part of the atmosphere does not correspond to the sub-stellar point i.e. the point of the planet's surface closest to the star. This is also observed in surface temperature mapping of the hot Jupiter HD 189733b obtained with Spitzer Space Telescope (Knutson et al., 2007a) shown in the right of Figure 1.9. Simulations of atmospheric circulation models find that this offset is caused by super-rotating equatorial jets which move the location of hottest point of the planet (e.g. Heng et al., 2015, and references therein).

The point of occultation, at which the planet is completely blocked by the star enables a baseline measurements for the star to be obtained without the planet. The depth of the occultation, is a direct measurement of the planet-to-star ratio between the star and the planet a **cite secondary eclipse of reflectance, and secondary spectroscopy examples.** Spectra obtained during the occultation will have no planetary signal and can be used remove the stellar component from spectra obtained at other phases to obtain the planetary spectrum.

The depth of the occultation is a measure of the flux from the day side of the planet which can indicate the atmospheric reflection and thermal emission of the planet's atmosphere.

1.3.2 Transmission spectroscopy

When a transiting planet crosses in-front of the host star it blocks out light from the star. However, a small portion light passes through the atmosphere of the planet as shown in Figure 1.10. The light that passes through the exoplanet atmosphere is partially absorbed, and is faintly imprinted with absorption

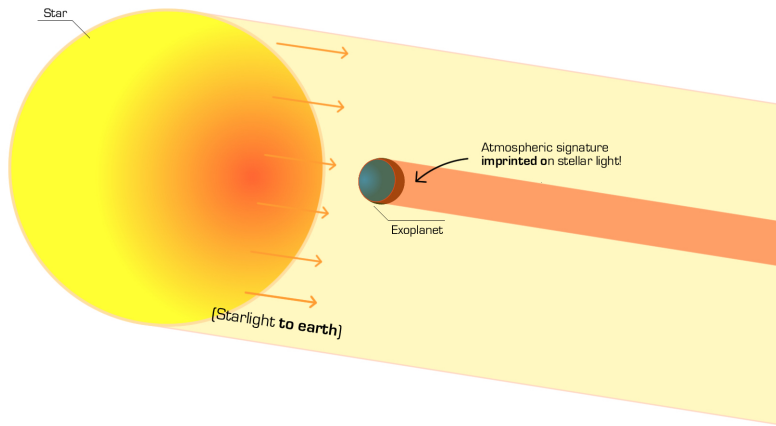


Figure 1.10: Diagram of transmission spectroscopy imprinting the atmosphere of the exoplanet. Sourced from <http://www.sc.eso.org/~esedagha/research.html>

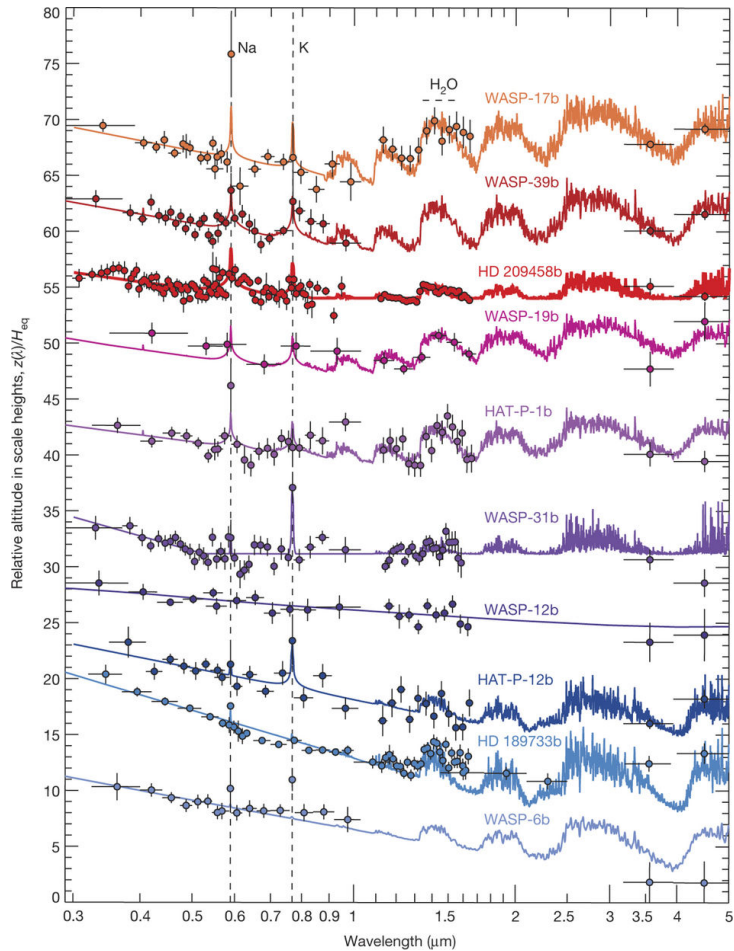


Figure 1.11: Transmission spectra (dots) for several Hot-Jupiter type exoplanets which increase in the amount of haze and clouds from top to bottom. The solid lines indicate the best fit atmospheric models. Credit Sing et al. (2016).

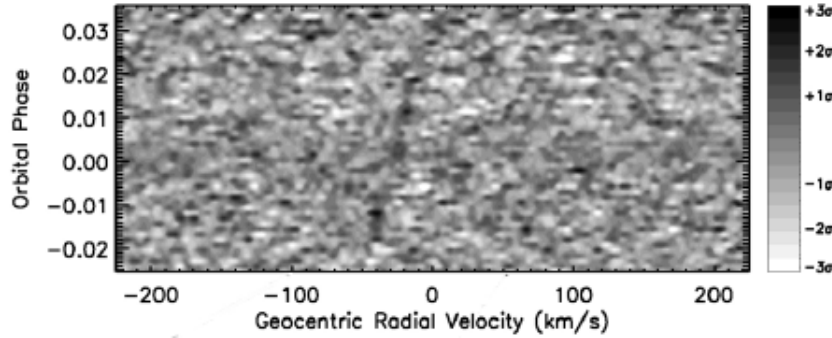


Figure 1.12: Cross-correlation signal of CRIRES observations during the transit of HD 209458 b with a CO template. Credit Snellen et al. (2010).

lines.

In planetary transits, usually defined by their duration and depth, there are degeneracies in the transit shape from a single band, such as the $\frac{R_p}{R_*}$ ratio. Observing transits in multiple bandpasses (i.e. by splitting the spectra observed during transits into several bands) has been shown to break the degeneracies between the stellar radius and the orbital inclination as well as determine the stellar limb darkening (Jha et al., 2000; Knutson et al., 2007b).

The radius of the transiting exoplanet can also appear to change size when observed at wavelengths where there is strong opacity in the atmosphere (e.g. Burrows et al., 2000; Seager et al., 2000). Which can be observed

The transmission spectra observed with space space observatories and ground based high resolution spectrographs have been able to detect several elements and molecules in the atmosphere. For example Na (Charbonneau et al., 2002; Redfield et al., 2008; Wyttenbach et al., 2015; Nikolov et al., 2016) H₂O (Tinetti et al., 2007; Brogi et al., 2014) CO (Brogi et al., 2014; Snellen et al., 2018), CH₄ (Redfield, 2010), Fe and Ti (Hoeijmakers et al., 2018). The presence of clouds in the atmosphere have also been detected, as they mask the atmospheric constituents as they produce wavelength-independent fluxes (e.g. Barman et al., 2011; Kreidberg et al., 2014; Sing et al., 2016).

Transmission spectra for several transiting Hot-Jupiter exoplanets from Sing et al. (2016) is shown in Figure 1.11. The amount of haze and clouds present in the atmospheres Increases from top to bottom. The clearer atmospheres near the top have large alkali (Na and K) and H₂O, while the cloudier planets lower down have strong optical scattering slopes, narrow alkali lines and partially or completely obscured H₂O absorption.

1.3.3 High resolution spectroscopy

Precise high resolution spectrographs, which are too large and bulky to fly in space, are able to spectrally resolve individual absorption lines, key for analysing the atmospheres of exoplanets. The large collecting area of current and future ground based telescopes make high resolution spectroscopy a great contender for obtained high-resolution observations for detecting and exploring exoplanetary atmospheres.

Typically high-resolution and high SNR are cross correlated with modelled planetary templates to recover the faint signal of the companion. This has been most successful in the nIR due to a the larger planet-to-star flux ratio notably with CRIRES, with the detection of orbital motion, atmospheric constituents and exoplanetary winds (e.g. Snellen et al., 2010; de Kok et al., 2013; Brogi et al., 2014; Brogi

et al., 2016; H. Schwarz et al., 2015). The rotation rate of exoplanets has been achieved by measuring the spectral line broadening (Snellen et al., 2014; Brogi et al., 2016). An example of a cross correlated result is given in Figure 1.12 showing the shift of the CO lines during a transit due to the orbital motion of the planet (Snellen et al., 2010).

The spectrum of the star and planet usually cannot be spatially resolved so methods to identify and remove the stellar component are required. This usually involves constructing a high SNR stellar mask from observations, possibly at different phases (e.g. Rodler et al., 2012), to subtract from the observed spectra leaving behind the planetary signal. If the planet is able to be spatially resolved, then a spectrum of the planet could be obtained without stellar contamination (e.g. Snellen et al., 2015).

High resolution spectroscopy of atmospheres is not limited to transit spectroscopy with detections also possible for non-transiting exoplanets (e.g. Brogi et al., 2012; Brogi et al., 2014; Lockwood et al., 2014; Piskorz et al., 2016).

An advantage of high-resolution spectra is that it allows the molecular absorption lines of Earth's atmosphere to be resolved. This way they can be identified and corrected/removed to avoid contamination with the atmosphere of the exoplanet. Lower resolution and photometric methods are unable to fully resolve and remove Earth's atmosphere from ground based observations.

1.4 From exoplanets to stars

Exoplanetary detections have challenged the theoretical formation models with their variety and distribution of sizes, locations. For instance, the discovery of the hot-Jupiter class (large mass planets on close in orbits) challenged the accepted planet formation theories at the time (e.g Pollack et al., 1996; Boss, 1997) in which our Solar System was thought to be typical with small rocky planets close to the Sun and large giant planets further away.

This needs a better title

The precise characterization of more exoplanets with the detection of exoplanetary atmospheres will allow for the constraints of exoplanetary composition and formation mechanisms to be improved. For instance, the core accretion model has been able to reproduce the large number of Super-Earths, the correlation between star metallicity and planet frequency (e.g. Santos et al., 2004; Fischer et al., 2005), and the presence of many Hot-Jupiter and Neptune in close-in orbits, with the help of migration mechanisms (e.g. Triaud, 2016). Recent models also combine both planetary formation and evolution to describe the observed exoplanets (e.g. Mordasini et al., 2012) and can reproduce general population properties in a statistically significant way (Mordasini et al., 2009).

A proxy for the composition and structure of an exoplanet is the average density, computed from the mass and radius. A mass-radius diagram is shown in Figure 1.13 for Earth-like rocky planets. The tracks show contours of mass-radius for different theoretical compositions (Brugger et al., 2017), while the circles indicate a number of detected small mass exoplanets, with K2-229 b being a Super-Earth with a Mercury-like density (Santerne et al., 2018). The density can give an approximate composition but for a given mass there are an infinite combinations of metal/silicate/ice and gas that can produce the same radii (e.g. Seager et al., 2007). Low mass planets tend to be rocky and tend to have small or no atmosphere. With rock being in-compressible, to first order, it is relatively insensitive to the incident flux. The radii of solid exoplanets are sensitive to gas content of the atmosphere as small increase in H/He can cause a large increase in radius (Adams et al., 2008).

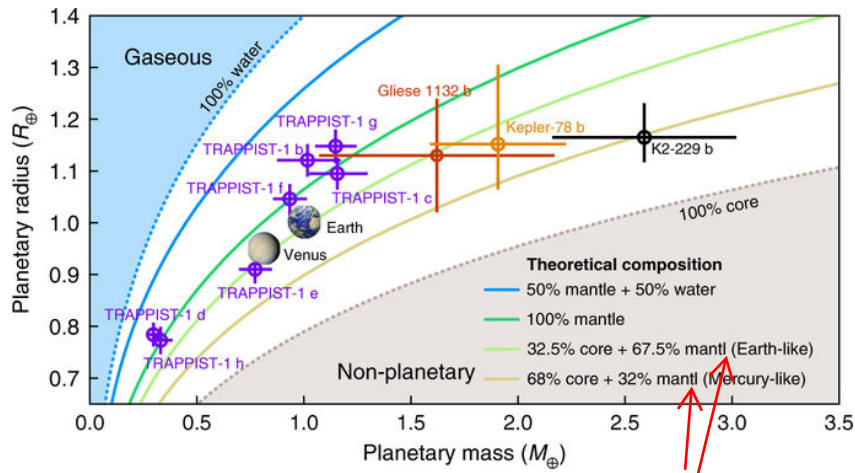


Figure 1.13: Mass-Radius diagram for rocky planets with composition contours. Adapted from Santerne et al. (2018)

When the gas component becomes dominate planets begin to have radii independent of their mass (e.g. Lopez et al., 2014). The atmospheres of gas giants are also susceptible to stellar irradiation, with close in Hot-Jupiters having inflated atmospheres and larger radii (e.g Fortney et al., 2010).

Models of the mass-radius relation are important as they enable insight into the likely planetary properties when only either mass or radius can or has been measured. For example Chen et al. (2016) develop a probabilistic model over 9 orders-of-magnitude in mass and 3 orders-of-magnitude in radius, with the result shown in Figure 1.14. There are four different power laws separate different with three different transition regions, also fitted by the model. This breaks the mass radius relation into different regions classified after a representative example from our solar system. The lowest mass range is the rocky "Terran" worlds up to $2.0 M_{\oplus}$ and inclusive of dwarf planets, "Neptunian" worlds between $2.0 M_{\oplus}$ and $0.41 M_{Jup}$, "Jovain" worlds between $0.41 M_{Jup}$ and $0.08 M_{\odot}$. With the transitions regions indicative of changing composition or physical processes (such as the hydrogen burning limit in stars) and consistent with other works (e.g. Weiss et al., 2013; Dieterich et al., 2014; Hatzes et al., 2015; Rogers, 2015).

When classified using just mass and size Chen et al. (2016) find no different between giant planets and Brown Dwarfs, with Brown Dwarfs being large giant planets.

Recently, there has been a renewed interest in Brown Dwarf (BD) candidates triggered by exoplanetary searches as they bridge the gap between giant planets and low-mass stars. It is difficult to distinguish between giant planets and BDs with a loosely suggested definition of mass between $13-80 M_{Jup}$ ¹¹ for Brown Dwarfs. This is between the Deuterium fusion mass of around $13 M_{Jup}$ (e.g. Spiegel et al., 2011) and the Hydrogen fusion limit of $80 M_{Jup}$ (Chabrier et al., 2000; Dieterich et al., 2014). Several works found similar properties on the two populations, like a similar density (Hatzes et al., 2015; Chen et al., 2016) seen in Figure 1.14 by the same power law spanning giant planets and BDs, while others have found intriguing differences.

There is a paucity of BD companions that exists in short period orbits around Sun-like stars ($\lesssim 5$ au), compared to stellar or planetary companions, termed the *brown dwarf desert* (Halbwachs et al., 2000; Zucker et al., 2001; Sahlmann et al., 2011; Ranc et al., 2015) which can be seen as the gap in the "Jovian" worlds section of Figure 1.14. There are observed differences in the host star metallicity (Maldonado

¹¹ $0.01-0.08 M_{\odot}$

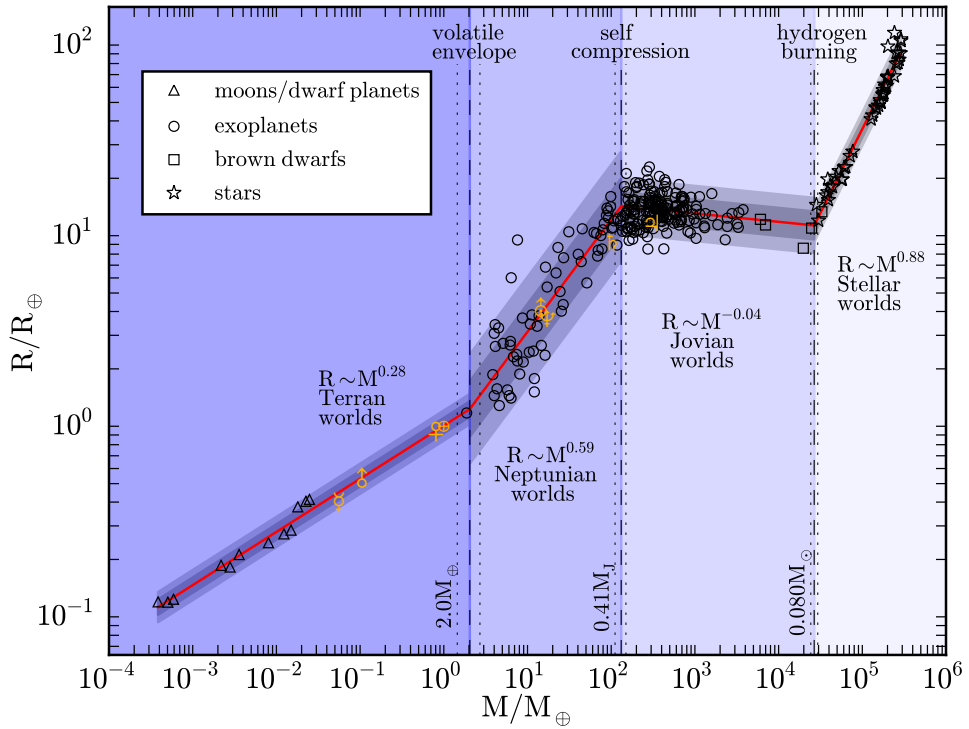


Figure 1.14: Left: Mass-Radius relationship with probabilistic fit from dwarf planets to late-type stars from Chen et al. (2016). The symbols represent the objects used to fit the model, with the key in the top-left. The red line indicates the average value, while the light and dark grey regions indicate the 65% and 95% confidence intervals.

et al., 2017; Santos et al., 2017; Schlaufman, 2018) and orbital eccentricity distribution (Ma et al., 2014) either side of the period/mass gap with the lower mass BDs more having properties similar to giant planets and high mass BDs having properties more like stars. There is a very strong hint of different formation mechanisms BDs below the gap may primarily forming via gravitational instability in protoplanetary disks, while above this gap BDs may form more like stellar binary from molecular cloud fragmentation (Ma et al., 2014).

As the number of known BDs orbiting solar type stars is low, the characterization of benchmark BDs in the brown dwarf desert (e.g. Crepp et al., 2016) is beneficial in understanding this sub-stellar population and to help constrain formation and evolution theories (Whitworth et al., 2007). There is an inherent degeneracy between the mass, age and luminosity of a given BD (Burrows et al., 1997) because without sustained fusion, BDs cool down over time with an age-dependent cooling rate.

BDs in binary systems, unlike free-floating BDs (e.g Gagné et al., 2017), allow for the determination of their masses, when complemented with radial velocity (RV) and astrometry measurements. The RV technique provides the mass lower-limit ($M_2 \sin i$) of binary and planetary companions, while complementary astrometry measurements can often provide mass upper-limits (e.g. Sahlmann et al., 2011). Measuring or tightening the constraints of BD masses improves the understanding of mass dependence on BD formation processes. Photometry along with stellar evolution models (e.g. Baraffe et al., 2003; Allard, 2013) can also be used to estimate the mass of BD companions (e.g. Moutou et al., 2017) if there is sufficient orbital separation, and a precise determination of the age (Soderblom, 2010).

Is this fine to leave it here

1.5 Motivation for this thesis

As shown here there is a vast field of exoplanet research, with one of the current challenges being the detection of planetary atmospheres. The purpose of this thesis was to develop methodologies and tools to extract the minute signals of planetary spectra from nIR spectra. With access to nIR spectra of stars with suspected Brown Dwarf companions¹² the higher temperature and relatively larger size of BDs compared to giant-planets makes the development of spectral recovery techniques for BD companions a logical step towards the spectroscopic detection of planetary atmospheres. For one, the spectrum of the BD companion will have a higher flux ratio than an exoplanet, and hence should be easier to detect. Secondly, being able to recover the spectra of these BD companions would help to constrain their mass and differentiate them from low-mass stars, helping to complete the puzzle regarding BD companions and their formation.

The original plan was to use this as a stepping stone to request observational time and apply the techniques on giant exoplanets in the nIR with the state-of-the-art detectors that are *still* in development. In Chapters 2 and 3 the fundamental concepts of the radial velocity method and nIR spectroscopy are presented. In Chapter 4 models of the atmosphere presented along with the stellar atmosphere and evolutionary models used in this work. The process of reducing nIR CRIRES spectra, with a comparison between two different reduction software is given in Chapter 5, followed by the post reduction calibration and atmosphere correction techniques required.

Chapter 6 presents spectral disentanglement techniques, focusing on the application of a differential subtraction technique to the nIR spectra of BD companions, as well as analysing the phase of the

¹² Only the minimum mass $M_2 \sin i$ known

observations obtained. A second technique is developed in Chapter 7 which attempts to fit the observations with a model comprised of two synthetic spectral components.

Towards a slightly different goal, Chapter 8 contains work computing the fundamental RV precision of M-dwarf in the nIR. These are the best candidates for detecting small mass planets in their habitable zone, and are a focus for upcoming nIR RV spectrographs. A focus was shifted towards updating the tools to compute the RV precision to prepare for the release of the CARMENES nIR spectral library.

Chapter 2

Fundamental Radial Velocity

The radial velocity method, has been a consistent powerhouse for the measurement of the orbital motion of binary stars and stars hosting exoplanets. In this chapter some of the key properties of Keplerian orbits and the RV signal will be presented along with an introduction to the notion of RV precision.

2.1 Keplerian Orbits

When two bodies are in orbit (two stars or a star and a planet) they orbit about their common centre of mass. Their 3-dimensional motion can be derived with a combination of Newton's universal law of gravitation, and Kepler's laws. The full derivation is quite long and can be commonly found in several celestial mechanics texts (e.g. Moulton, 1914; M. Perryman, 2011; Fitzpatrick, 2012). The notes given here mainly follow (Bozza et al., 2016).

Figure 2.1 shows the basic elements of the Keplerian orbit. There are several parameters required to situate the orbit in space. There is a *reference plane*, tangential to the celestial sphere, that cuts the orbital plane with a *line of nodes*. The *ascending node* is the point on the plane at which the body crosses the reference plane moving away from the observer, and is defined relative to the vernal reference point, Υ , with the *longitude of the ascending node*, Ω , setting the orientation.

To fully parametrize a Keplerian orbit requires seven parameters. These are: a the semi-major axis of the elliptical orbit, e the orbital eccentricity, P orbital period, T_0 the *time of periastron passage*, i orbital inclination relative to the line of sight, ω the *argument of periastron*, and Ω . From RV measurements alone all of these parameters except for i and Ω can be determined. Ω is irrelevant for determining the orbital mass, but inclination i is very important as it effects the projection of the velocity towards the observer.

With a two body system with masses M_1 and M_2 , under the force of gravity, their orbits are elliptical *orbit* about their barycentre mass, as seen in Figure 2.2. In polar coordinates the ellipse of an orbit about the centre of mass (located at the focus F_1) is described by:

$$r = \frac{a(1 - e^2)}{1 + e \cos \nu(t)}, \quad (2.1)$$

where a is the length of the semi-major axis for the body, e is the eccentricity, ν is the *true anomaly* the

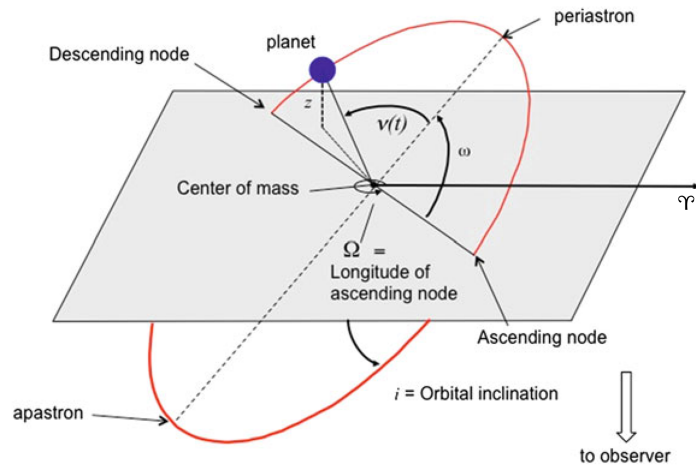


Figure 2.1: The basic elements of the Keplerian orbit. Adapted from (Bozza et al., 2016).

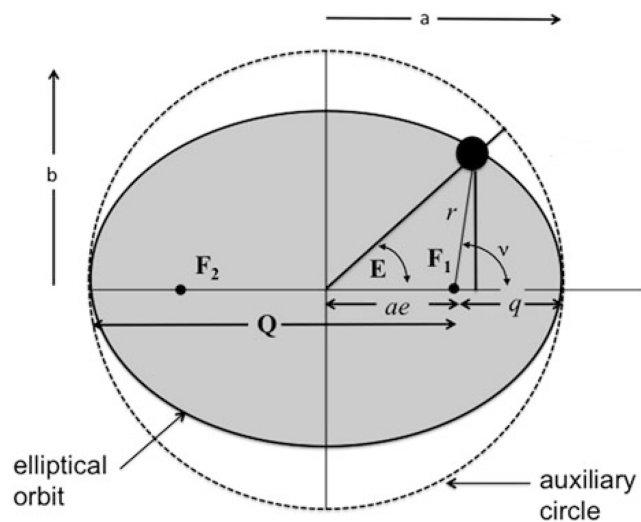


Figure 2.2: Elements of an elliptical orbit about the common centre of mass F_1 . ν is the angle to the position of the orbiting body from the periapse (closest point to barycentre). The auxiliary circle has a radius equal to the semi-major axis of the ellipse. Adapted from (Bozza et al., 2016).

angle between the current position of the orbiting body and periastron.

The true anomaly is not only a function time, t , but also the orbital period P , the *time of periastron passage*, T_0 , and eccentricity. It is geometrically related to the eccentric anomaly:

$$\cos \nu(t) = \frac{\cos E(t)}{1 - e \cos E(t)} \quad (2.2)$$

which can be numerically determined from the mean anomaly $M(t)$:

$$M(t) = \frac{2\pi}{P}(t - T_0) = E(t) - e \sin E(t) \quad (2.3)$$

The mean anomaly is the angle for the average orbital motion of the body at a time after periastron passage $t - T_0$.

From Kepler's second law¹ $\frac{1}{2}r^2 d\nu/dt = \text{constant}$, while in one full period P , the total area of the ellipse $\pi a^2(1 - e^2)^{1/2}$ will be covered, leading to:

$$r^2 \frac{d\nu}{dt} = \frac{2\pi a^2(1 - e^2)^{1/2}}{P} \quad (2.4)$$

The radial velocity is the change in r along the line of sight z . The component of r along the line of sight (from Figure 2.1) is:

$$r_z = r_1 \sin(\nu_1(t) + \omega) \sin i + \gamma \quad (2.5)$$

where γ is the mean velocity of the barycentre, and the subscripts '1' and '2' refer to the star and planet (or companion star), respectively. Differentiating Equation 2.5 and substituting in Equation 2.4 leaves the common RV equation:

$$RV = \dot{r}_z = \frac{2\pi a_1 \sin i}{P(1 - e^2)^{1/2}} [\cos(\nu(t) + \omega) + e \cos \omega] + \gamma \quad (2.6)$$

$$= K_1 [\cos(\nu(t) + \omega) + e \cos \omega] + \gamma, \quad (2.7)$$

where several parameters and constants have been condensed into K , referred to as the *semi amplitude*. In this case K_1 is the semi amplitude for the star.

2.1.1 Mass function

Once the orbital parameters have been determined then it is possible to determine the mass function of the system. From the centre of mass the distance between the two bodies is $a = a_1 + a_2$ where a_1 and a_2 are the respective distances to the barycentre, while the value $M_1 a_1 = M_2 a_2$ can allow these re-arrangements:

$$a = a_1 \left(1 + \frac{a_2}{a_1}\right) = a_1 \left(1 + \frac{M_1}{M_2}\right) = \frac{a_1}{M_2} (M_1 + M_2) \quad (2.8)$$

¹ Orbit sweeps out equal areas in equal times

Table 2.1: The RV semi-amplitude induced by the planets with different masses and periods around a $1 M_{\odot}$ -mass star.

M_2	$K_1(P = 3 \text{ d})$	$K_1(P = 1 \text{ yr})$	$K_1(P = 5 \text{ yr})$	
M_{Jup}	140.8	28.4	16.6	m s^{-1}
M_{Nep}	7.60	1.53	0.90	m s^{-1}
M_{\odot}	44.3	8.9	5.2	cm s^{-1}

Kepler's third law ($G(M_1 + M_2)/4\pi^2 = a^3/P^2$) can be written as:

$$\frac{G(M_1 + M_2)}{4\pi^2} = \frac{a_1^3}{P^2} \left(\frac{M_1 + M_2}{M_2} \right)^3 \quad (2.9)$$

replacing a_1 with K_1 from Equation 2.6 results in the *mass function*, $f(M)$:

$$f(M) = \frac{(M_2 \sin i)^3}{(M_1 + M_2)^2} = \frac{K_1^3 P (1 - e^2)^{3/2}}{2\pi G} \quad (2.10)$$

This function can be determined directly from the measurable parameters P , e and K_1 . It also depends on the stellar mass M_1 , which needs to be measured by some other means to determine the planet mass. Also from this function that the true mass of the planet M_2 is not obtained but only the projected mass $M_2 \sin i$.

For a planetary companion the approximation $M_2 \ll M_1$ can be made and for circular orbit the radial velocity semi-amplitude can be re-written as:

$$K_1 = \frac{28.4}{\sqrt{1 - e^2}} \frac{M_2 \sin i}{M_{\text{Jup}}} \left(\frac{M_1}{M_{\odot}} \right)^{-2/3} \left(\frac{P}{1 \text{ yr}} \right)^{-1/3} [\text{m s}^{-1}] \quad (2.11)$$

This can be used to calculate the RV amplitude created by different mass planets in various circular orbits as given in Table 2.1.

If there is more than one companion/planet then there will be a gravitational influence between each other and their orbits become non-Keplerian, i.e. a N-body problem (e.g. Chenciner, 2007). Assuming that the gravitational influence between companions is negligible the RV signal observed in the host star can be treated as just a sum of tugs from each companion. For the two instances in this work where the target star has two companions, the companions will be treated separately, as if they were alone.

2.1.2 Binary mass ratio

In the above equation RV of the companion has not yet been addressed. Equation 2.6 above is the RV of the star in an elliptical orbit around the centre of mass between it and its companion. Similarly the elliptical orbit of the planet around the centre of mass is given by:

$$RV_2 = K_2 [\cos(\nu(t) + \omega_2) + e \cos(\omega_2)] + \gamma, \quad (2.12)$$

where $\omega_2 = \omega + 180^\circ$ due to the phase difference between the two components, resulting in the relative velocity (ignoring γ) of the companion being opposite the star and:

$$K_2 = \left(\frac{2\pi G}{P(1 - e^2)^{3/2}} \right)^{1/3} \frac{M_1 \sin i}{(M_1 + M_2)^{2/3}} = \frac{2\pi a_2 \sin i}{P(1 - e^2)^{1/2}} \quad (2.13)$$

The orbits of the host and companion are directly related through the mass ratio of the star and companion:

$$q = \frac{M_2}{M_1} = \frac{K_1}{K_2} = \frac{RV_1}{RV_2} = \frac{r_2}{r_1}. \quad (2.14)$$

Typically in exoplanet detections the companion (planet) is too faint to measure the planetary velocity. However in double lined spectroscopic binary the spectrum of both stars can be identified in the blended spectra and the RV of both star and companion can be measured and monitored over the orbit. With both velocities the mass ratio of the binary can be found. The individual masses however is still not determinable due to the inclination $\sin i$ of the orbit.

In Chapter 6 the detection of the faint spectra is of known companions is attempted, in order to determine the velocity change of the companion and hence the mass ratio. To help with the analysis and simulations the known orbital parameters (see Tables 6.1 and 6.2) are used along with the companion mass (M_2 or $M_2 \sin i$) to predict or estimate the RV of the companion using Equations 2.12 and 2.14. Note, that for the targets in which only the minimum mass ($M_2 \sin i$) is known and used in the mass ratio, this will result in the maximum RV semi amplitude for the companions orbit. The estimated K_2 for each companion is provided in Table 6.4 while the RV for both components at the time of each observation is provided in Table 6.3.

I think this is finished

2.2 Measuring the RV

Slight motion of the spectral lines on the detector. To use the information from the whole spectrum the cross correlation is common to add all the lines together into a single line. see. ..

something about measuring the RV and CCF

This then becomes a property of the spectrum such as line density and number of deep strong lines.

Transition into precision.

2.3 Radial velocity precision

The first detections of extrasolar planets with the RV technique were hot-Jupiters; Jupiter mass planets in close orbits to their star. The RV precision required to detect the first hot-Jupiter, 51 Peg b, was Mayor et al., 1995 using Since that time the instrumental development and the detection and observation techniques have been refined to achieve RV precisions better than 1 m s^{-1} . The recently commissioned ESPRESSO optical spectrograph is designed with the goal of achieving 10 cm s^{-1} , which is the level of precision required to detect an Earth mass planet in an 1 year orbit round a Sun-like star.

find mayor queloz precision achieved
what reference

Over the years the community has pushed the limits of this technique to smaller and smaller planetary masses. An example is shown in Figure 2.3.